

# Comprehensive Anisotropic Linear Optical Properties of Weyl Semimetals, TaAs and NbAs

Rui Zu,<sup>1</sup> Mingqiang Gu,<sup>6,\*</sup> Lujin Min,<sup>1</sup> Chaowei Hu,<sup>5</sup> Ni Ni,<sup>5</sup> Zhiqiang Mao,<sup>2</sup> James M. Rondinelli,<sup>4</sup> Venkatraman Gopalan<sup>1,2,3,†</sup>

<sup>1</sup>*Department of Materials Science and Engineering, Pennsylvania State University, University Park, Pennsylvania, 16802, USA*

<sup>2</sup>*Department of Physics, Pennsylvania State University, University Park, Pennsylvania, 16802, USA*

<sup>3</sup>*Department of Engineering Science and Mechanics, Pennsylvania State University, University Park, Pennsylvania, 16802, USA*

<sup>4</sup>*Department of Materials Science and Engineering, Northwestern University, Evanston, Illinois, 60208, USA*

<sup>5</sup>*Physics and Astronomy Department, University of California, Los Angeles, Los Angeles, California, 90095, USA*

<sup>6</sup>*Shenzhen Institute for Quantum Science and Engineering (SIQSE) and Department of Physics, Southern University of Science and Technology, Shenzhen 518055, China*

Since the experimental discovery of Weyl semimetals, they have attracted significant attention owing to their unique band structure and the chirality of their Weyl points. TaAs and NbAs are two of the earliest identified Weyl semimetals that possess broken inversion symmetry. Linear and nonlinear optics have been employed as tools to probe the Weyl physics in these crystals. Although some literature exists on their linear optical properties, a comprehensive study of its complete anisotropic dielectric function is presently missing. Here, we use eigen-cut crystals to fully determine the complete anisotropic dielectric functions of TaAs and NbAs by combining spectroscopic ellipsometry and density functional theory (DFT). Parameterized Lorentz oscillators are reported from 1.2-6 eV (experiment) and 0-6 eV (DFT). Strong resonances are found below 1 eV, which originate from Ta ( $5d$ ) to Ta ( $5d$ ) and As ( $4p$ ) to Ta ( $5d$ ) transitions. Given the popular laser wavelengths of 0.7, 1.55, and 3.1 eV, optical transitions near these energies are examined. The contribution of the band structure in the proximity of the Weyl cones to the total linear dielectric function is quantified relative to the contribution from the rest of the Brillouin zone. This analysis shows that the Weyl points contribution to the total dielectric function is highly anisotropic and rises below 0.5 eV; however, these contributions are negligible above 1 eV.

## I. INTRODUCTION

Although Weyl fermion was initially predicted in high energy physics [1], it was first experimentally discovered in condensed matter, namely the TaAs family [2]. Weyl fermions can

\*[gumq@sustech.edu.cn](mailto:gumq@sustech.edu.cn)

†[vxg8@psu.edu](mailto:vxg8@psu.edu)

be described as low-energy excitations near the Weyl nodes which represent the crossing points of singly-degenerate bands in the presence of broken inversion symmetry or broken time-reversal symmetry. Weyl nodes appear in pairs with opposite chiralities; the bulk and surface state correspondence results in surface Fermi arcs. All these hallmarks of Weyl states have been demonstrated experimentally [3–10]. Weyl fermions give rise to a wide range of exotic transport properties [11], such as extremely high mobility [12], negative longitudinal magnetoresistance caused by chiral anomaly [13], and intrinsic anomalous Hall effect [14–17].

Optical measurements have been used as a powerful technique to characterize the exotic properties of Weyl semimetal states. [18–22] To explore the linear band crossing near the Fermi level, the temperature-dependent Drude behavior in the low energy range and linear optical conductivity near the Weyl points have been explored. [23–25] The optical transitions in TaAs near the two types of Weyl nodes (labeled W1 and W2) have been identified to be  $<0.1$  eV (for W1) and  $<0.2$  eV (for W2). [24] Due to the intrinsic noncentrosymmetry in the TaAs family, strongly anisotropic second harmonic (SHG) and circular polarized galvanic effect (CPGE) have been observed, prompting further interest in higher-order nonlinear and coupled optical properties. [18,26] The giant SHG response in the TaAs family has been attributed to linear resonances, as well as the shift current. [26–29] While extensive studies have focused on exploring the spectroscopic behavior at energies near Weyl points [19,20,24], and the optical resonances that contribute to giant SHG [27], the complete *anisotropic* linear optical susceptibility tensor, *anisotropic* complex refractive indices, and the band- and momentum- resolved optical transitions in TaAs and NbAs across the visible and near-infrared spectrum remain unreported. To that end, we report the complete anisotropic linear optical properties of both TaAs and NbAs, and discuss the consequences of anisotropy in utilizing optical probes for probing Weyl physics.

Unlike previous studies which were confined to the natural (112) planes of the crystal, in this work, we cut crystals perpendicular to the various eigendirections to directly probe properties along the principal axes and study the anisotropic linear optical properties and resonances in TaAs and NbAs. Large anisotropic optical dielectric resonances are found below 3.5 eV. The complete parameterized Lorentz oscillators within 1.2-6 eV (experiment, Expt.) and 0-6 eV (DFT) are reported, corresponding to interband transitions. Strong resonances are found below 1 eV between the first two conduction and valence bands near the Fermi level, which originate from Ta ( $5d$ ) to Ta ( $5d$ ) and As ( $4p$ ) to Ta ( $5d$ ) transitions. Resonances are observed near the energies where previous optical second harmonic generation (SHG) experiments were performed [26,27]; they are expected to enhance the SHG effect. The contribution from the Weyl points to the dielectric function is also quantified; we find Weyl contributions are significant at low energy, below 0.5 eV, and are negligible at energies greater than 1 eV, indicating low-energy optical probes are required to discern topological band features in the TaAs family.

## II. METHODS

TaAs and NbAs exhibit a similar crystal structure (**Fig. S1(a)**) and the same point group  $4mm$  ( $a = 3.4348\text{\AA}$ ,  $c = 11.641\text{\AA}$  for TaAs;  $a = 3.452\text{\AA}$ ,  $c = 11.679\text{\AA}$  for NbAs;  $c$ -axis in both cases is parallel to the [001] direction). [30,31] Single crystals of TaAs and NbAs were grown by chemical vapor transport with stoichiometrically mixed Ta (or Nb) and As powders at around 1000°C for four weeks (details can be found in SI). As-grown surfaces of (020) are determined by  $\theta - 2\theta$  X-ray diffraction confirming single-crystalline properties and (020) out-of-plane direction (See **Fig. S2**). The in-plane [001] and [100] directions are then determined by Laue backscattering diffraction and confirmed by the electron backscatter diffraction (EBSD) (See **Fig. S3**).

Crystal quality plays a vital role in the intrinsic properties such as vacancies and stacking faults, which could shift the positions of Weyl nodes and alter the Fermi surface [32]. A previous study [33] shows that the Weyl nodes move closer to the Fermi level as the mobility increases. The quality of the studied crystals is examined using Hall measurements (**Fig. S4**). Analysis of the transport data show that the electron mobility of TaAs is  $\mu_e(10K) = 6.04 \text{ m}^2\text{V}^{-1}\text{s}^{-1}$  and for the NbAs to be  $\mu_e(10K) = 83.5 \text{ m}^2\text{V}^{-1}\text{s}^{-1}$ , which is comparable to that reported in the literature. [34–37] Thus, the above properties suggest that the crystals studied here are reasonable representatives of the crystals reported in the literature.

Spectroscopic ellipsometry is performed using Woollam M-2000F focused beam spectroscopic ellipsometer with wavelengths from 1000 nm (1.2 eV) to 200 nm (6 eV). Amplitude change and phase shift of the specularly reflected light are collected as a function of the wavelength, which is sensitive to the crystal orientations. Three different orientations are measured and fitted simultaneously with the Lorentz model to confirm the uniqueness of the model. The complex dielectric permittivity tensor for the uniaxial system is given by the diagonal second rank tensor,  $\tilde{\epsilon} = (\tilde{\epsilon}_{11} = \tilde{\epsilon}_{22}, \tilde{\epsilon}_{33})$ , where subscripts 1 and 3 denote crystallographic  $a$  and  $c$  axis. The three different crystal cuts used in this study are represented as orientation **A**: [001] // lab  $x$ , [010] // lab  $z$ ; orientation **B**: [001]// lab  $y$ , [010]// lab  $z$  and orientation **C**: [1 -1 0]// lab  $x$ , (112)// lab  $z$  respectively where the  $x$ - $z$  plane is the plane of incidence. Kramers-Kronig relationship between real and imaginary components of the dielectric tensor is imposed during the modeling of the ellipsometry data. The imaginary component of the dielectric function is forced to be positive in all the fittings.

Density functional theory (DFT) calculations are performed using Vienna Ab-initio Simulation Package (VASP) [38] to provide insights into the electronic properties leading to the

optical dielectric function. The Perdew-Burke-Ernzerhof (PBE) functionals [39] with spin-orbital coupling (SOC) interactions are used in all calculations with a planewave expansion up to 500 eV. The projector augmented wave (PAW) method [40] is used to treat the core and the valence electrons using the following electronic configurations:  $5p^6 6s^2 5d^3$  for Ta,  $4p^6 5s^2 4d^3$  for Nb, and  $4s^2 4p^3$  for As. A  $30 \times 30 \times 30$   $\Gamma$ -centered Monkhorst-Pack  $k$ -point mesh is used for calculating the electron density of states (DOS) and the optical properties. A smearing factor of 0.02 eV is employed for the  $k$ -point summation. To evaluate the contribution of the dielectric functions from the Weyl points, we used dense  $k$ -point grids and calculated the dielectric functions from the vicinity of the Weyl points, i.e., a  $\frac{K_a \times K_b \times K_c}{20^3}$  cube centered at either WP1 or WP2.

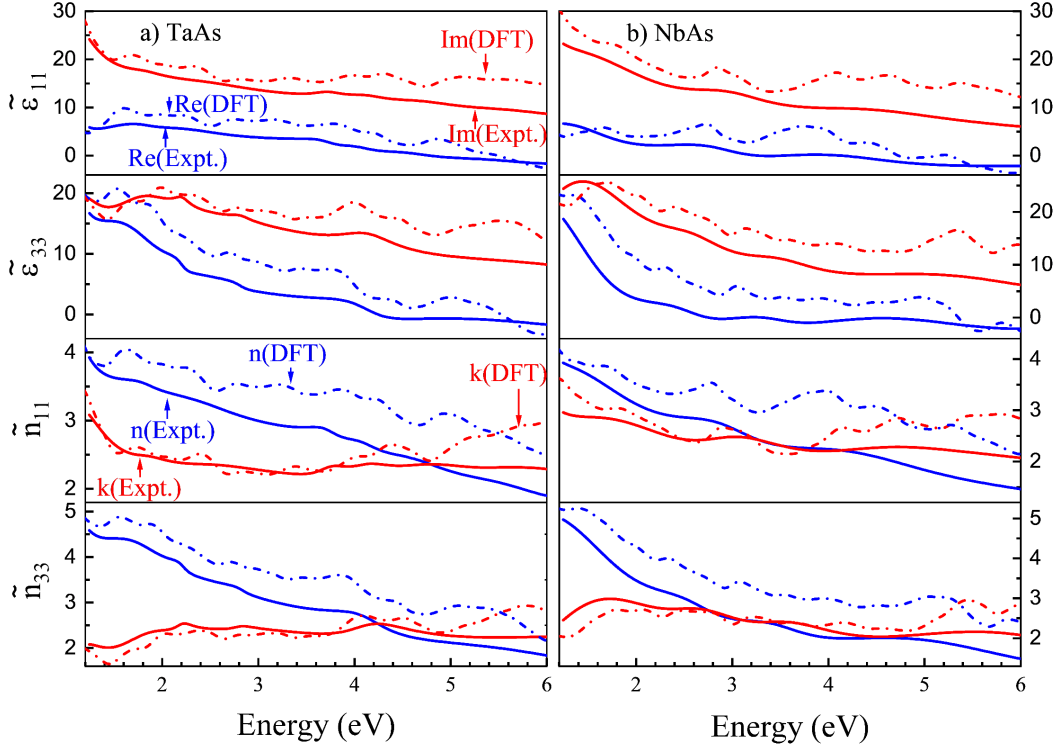


FIG 1. The complex dielectric functions  $\tilde{\epsilon}_r$  and refractive indices  $\tilde{n} = n + ik$  of (a) TaAs and (b) NbAs. The solid line and dashed line represent the experiment (Expt.) and DFT, respectively. The blue and red curves are the real (Re) and imaginary (Im) components of the dielectric constant

$\tilde{\epsilon}$  and refractive index  $\tilde{n}$ . Subscripts 1 and 3 indicate directions along ordinary and extraordinary eigendirections.

### III. RESULTS AND DISCUSSION

#### A. Anisotropic Dielectric Tensor: Experiments and DFT

The complex dielectric function  $\tilde{\epsilon}_r$  and refractive index  $\tilde{n}$  obtained from both ellipsometry and DFT is shown in **Fig. 1**. The experimental and calculated results show a reasonable agreement in terms of the trends, magnitudes, and resonance frequencies. The plasma edge determined by previous studies is below 0.1 eV [23,25]. Therefore, in the visible range, the dielectric function is dominated by interband transitions. The Drude behavior will have a limited impact on the modeling and will not influence the resonance energies in the energy range probed by ellipsometry. To capture the resonances from 1.2 eV to 6 eV, the Lorentz model is used to simulate phase and intensity changes of the reflected light in the ellipsometry data as shown below [26],

$$\tilde{\epsilon} = \epsilon_{\infty} + \sum_n^N \frac{A_n \Gamma_n E_n}{E_n^2 - E^2 - i \Gamma_n E} + \frac{A_{UV}}{E_{UV}^2 - E^2} + \frac{A_{IR}}{E^2} \quad (1)$$

where  $A_n$ ,  $\Gamma_n$ , and  $E_n$  are the resonance amplitude, broadening, and energies, respectively, of each oscillator labeled by  $n$ , and  $\epsilon_{\infty}$  represents the dielectric constant in the infinite frequency limit. Subscripts UV and IR are used as deep-ultraviolet and infrared poles, respectively, beyond the fitting spectrum. In TaAs, eight oscillators are captured along the crystallographic  $a$  axis and seven oscillators are captured along the  $c$  axis. The detailed fitting parameters for oscillators are shown in **Tables A.I** (for the ordinary component) and **A.II** (for the extraordinary component) for TaAs, and in **Tables A.III** (for the ordinary component) and **A.IV** (for the extraordinary component) for NbAs.

It is found that within 1.2 eV to 6 eV,  $k$  decreases slower than  $n$  and gradually exceeds the real component. Thus, with an increase in the photon energy, the reflectivities of TaAs and NbAs decrease, in agreement with previous literature [23], while the absorption coefficients show much less dispersion with energy. However, near the measured spectrum edges (below 1.2 eV and above 6 eV), the oscillators are not fully captured, and only the tails of resonances can be observed. Therefore, the resonance energies of the first and last oscillators along each of the eigendirections are set slightly beyond the spectrum to simulate the resonance near the spectrum edge. Although the overall dielectric function for the experiment and the DFT agree, the broadening parameters,  $\Gamma_n$  in **Eq. (1)** are larger for the experimental resonances than for the DFT resonances, which obscure the details of several DFT resonances that may appear to be merged together under an experimental resonance.

Having shown the overall broad agreement between experiments and theory in **Fig. 1**, and given that the DFT can shed light on the electronic transitions at energies of relevance, we next focus our discussions below on the DFT resonances. The linear dielectric functions from DFT are fitted from 0 to 6 eV using **Eq. (1)**. The complete set of Expt. and DFT oscillators from 1.2-6 eV and 0-6 eV for TaAs are shown in **Fig. 2** (See **Fig. B1** for NbAs), and detailed fitting parameters are shown in **Tables A. I-IV**. The black curve shows the total  $\epsilon''$  and the colored curves represent the fitted oscillators. Around 16 oscillators are located along each eigendirection across the fitting spectrum from 0-6 eV. A resonance dominates the dielectric constant at  $\sim 0.2$  eV along the ordinary direction, close to the saddle points between pairs of the Weyl points [24]. This indicates a strong optical transition near the Weyl points at low energy and can be associated with transitions from the lower Weyl bands (LWB) to the energy states above the upper Weyl bands (UWB) at WP2.

The resonances captured by experiments (Expt.) and density functional theory (DFT) show an excellent qualitative match and a reasonable quantitative match. In **Fig. 2(a)**, resonances in experiments (Expt.) and DFT at similar energies are mapped with the same colors; this mapping should be taken as approximate guides to the eye and not as a strict many-to-one mapping. Along the ordinary direction, experimental oscillators at 1.0, 1.8, 3.7, and 4.1 eV can be approximately one-to-one mapped with DFT oscillators at 1.1, 1.7, 3.9, and 4.4 eV, respectively. The experimental oscillator at 2.9 eV has a large broadening parameter,  $\Gamma$ , and it can be mapped as a collection of multiple narrower resonances seen in DFT. The resonance at 2.9 eV (Expt.) can possibly be composed of four different oscillators (DFT) at 2.1, 2.4, 2.8, and 3.4 eV. Along the extraordinary direction, experimental oscillators at 1.2, 1.8, 2.2 and 2.8 eV can be mapped to the DFT resonances at 1.1, 1.7, 2.0 and 2.8 eV, as shown in **Fig. 2(b)**. Similar to the broad resonance observed at 2.9 eV (Expt.) along the ordinary direction, the experimental oscillator at 3.0 eV possesses a large broadening parameter and hence a large linewidth, perhaps composed of densely-spaced resonances of 2.4, 3.0, 3.2, 3.5 and 4.0 eV as color-coded in blue in **Fig. 2(b)**.



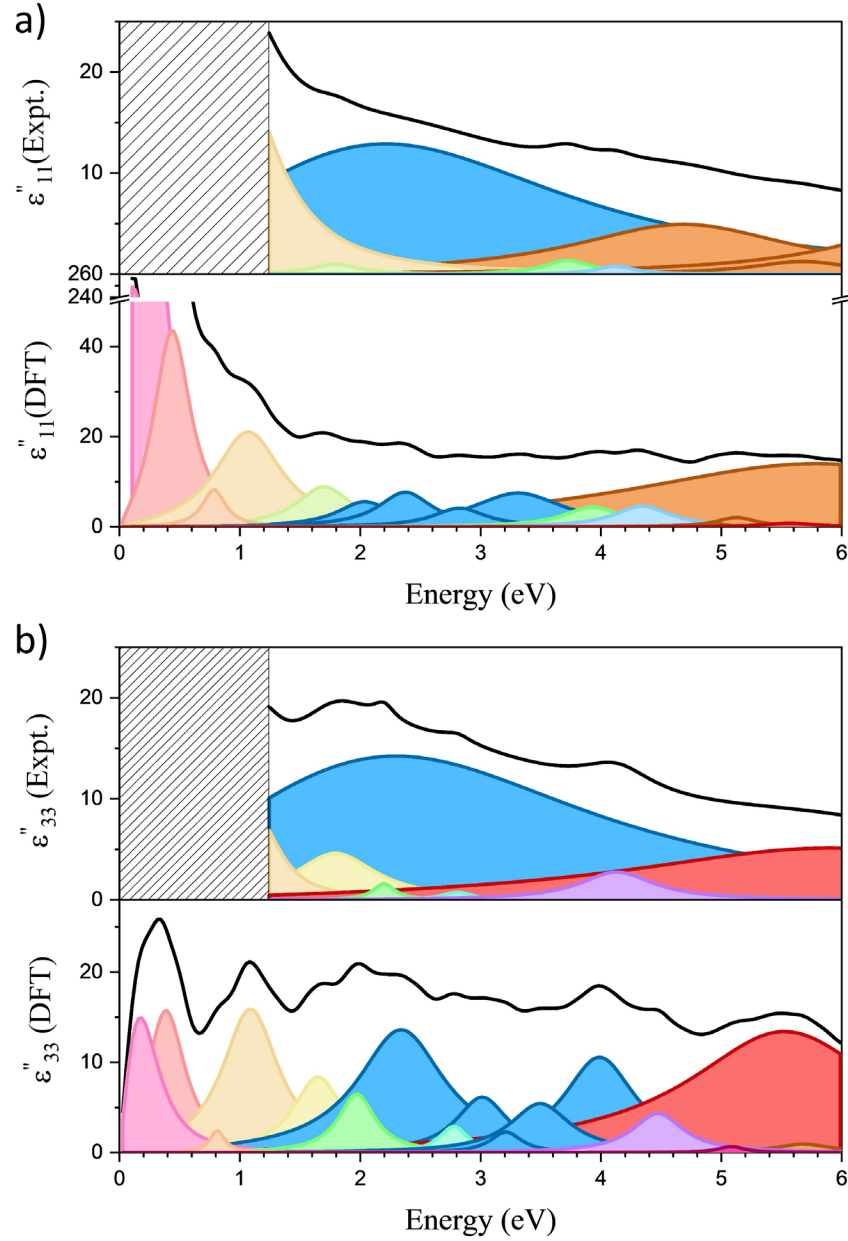


FIG 2. Detailed Lorentz oscillators for TaAs obtained from both experiment and DFT. a) Ordinary imaginary dielectric function. The hatched area indicates the energy range beyond the experimentally measured spectrum. b) Extraordinary imaginary dielectric function. The black curve is the total imaginary dielectric function. Colored curves represent individual oscillators. In each subplot, similar colors of oscillators are approximate many-to-one mapping from theory to

experiments; such mapping should not be strictly interpreted but only as a general guide to the eye as described in the main text. The resonance energies and linewidths are given in **Tables A. I-II**.

## B. Band Structure and Optical Transitions

Since the optical excitation occurs across the bands throughout the entire Brillouin zone (BZ), both transitions from the non-topological bands and the topological (Weyl) bands are reflected in the total dielectric spectrum, and care is needed in distinguishing their independent contributions. To understand the optical dielectric functions plotted in **Figs.1** and **2**, we carefully examine the electronic band structure and the optical transition matrix elements. With the confidence in the DFT calculated dielectric function based on its reasonable comparison with experiments (**Figure 1**), we next proceed to look carefully at the microscopics.

In **Fig. 3(a)**, the calculated DFT-SOC band structure, and the resulting density of states for TaAs are shown (the corresponding figure for the band structure and the density of states for NbAs are shown in **Appendix B, Figure B1**). Here, V1-8 and C1-8 are sequentially numbered valence and conduction bands, respectively, in the figures. Two different Weyl points (WP1 and WP2) were previously identified to be located along the  $\Gamma - \Sigma$  and  $\Sigma - \Sigma_1$  directions, in the absence of SOC (See **Fig. S1(b)** for high symmetry points). [2,41] When SOC is taken into account, the lines of Weyl nodes are further decomposed into 12 pairs of Weyl nodes, four pairs of WP1, and eight pairs of WP2. [42] Mirror symmetry protects each pair of Weyl points. The  $k$ -space momenta for WP1 and WP2 are calculated to be (0.015, 0.925, 0.004) and (0.505, 0.034, 0.313), where  $k_x$ ,  $k_y$  and  $k_z$  are parallel to the crystallographic  $a$ ,  $b$ ,  $c$  axes respectively. In the vicinity of the Fermi level, the states are mostly contributed by the hybridized Ta ( $d$ ) orbital, while the states provided by As ( $p$ ) are concentrated near the Z point. Deep within the valence band, the states are mostly As ( $p$ ) character. The conduction band is mostly composed of Ta ( $d$ ) orbitals. In the case of optical

excitation in the infrared (IR) and visible regimes, optical excitations in TaAs are dominated by Ta (*d*) to Ta (*d*) and As (*p*) to Ta (*d*) transitions.

To connect the macroscopic Lorentz resonances with the optical transitions in the band structure, we then evaluate theoretical resonances and *k*-dependent direct transitions. Here we focus on the oscillators below 3.5 eV, where most experimental optical characterizations are performed. The linear spectroscopic susceptibility is determined by electric dipole transition moments and their resonant and anti-resonant states expressed as, [43]

$$\chi_{ij}^{(1)}(\omega_p) = \frac{N}{\epsilon_0 \hbar} \sum_n \left( \frac{\mu_{an}^i \mu_{na}^j}{(\omega_{na} - \omega_p) - i\gamma_{na}} + \frac{\mu_{na}^j \mu_{an}^i}{(\omega_{na} + \omega_p) + i\gamma_{na}} \right) \quad (2)$$

where  $\omega_{na} \equiv \omega_n - \omega_a$  and  $\chi_{ij}^{(1)}$ ,  $\mu$ ,  $\omega$ ,  $N$ , and  $\gamma$  are the anisotropic susceptibility, electric dipole transition moment, photon frequency, the number density of atoms, and decay rate related to the damping term. Here, *n* and *a* represent the excited and ground states. The pairs of bands contributing most to the dielectric functions are calculated using **Eq. (2)** and plotted in **Fig. 3(b)**, **(c)**, and **(d)**. The dielectric function contribution generated by a certain momentum path in *k*-space was calculated by summing the contributions of every transition matrix element within the path for a specific energy. In particular, the  $|\tilde{\epsilon}|$  of a particular pair of bands within a momentum path was evaluated by fixing the bands, *n* and *a*, in **Eq. (2)** and summed over the transition matrix elements between these bands along the path.

The colored rectangles in **Fig. 3(b)** show the *k* space that predominantly contributes to a specific dielectric constant. For example, the blue rectangles shown in the  $\Gamma - \Sigma$ ,  $\Sigma_1 - Z$ , and  $Z - \Gamma$  indicate the pairs of bands that contribute most to  $|\tilde{\epsilon}_{11}|$  within the energy range covered by the rectangles. Similarly, the orange rectangles depict the bands contributing predominantly to  $|\tilde{\epsilon}_{33}|$ . The dark green (addition of the above blue and orange colors) rectangles depict pairs of bands

contributing to both  $|\tilde{\epsilon}_{11}|$  and  $|\tilde{\epsilon}_{33}|$ . The remaining energy regions not included by the colored rectangles in panel 3(b) do not have any predominant  $k$  space that contributes to the  $|\tilde{\epsilon}|$  at that energy; all five symmetry paths bands contribute similarly.

Along the ordinary direction of TaAs, 15 oscillators are fitted to the DFT derived dielectric function,  $|\tilde{\epsilon}_{11}|$ . At  $\sim 0.2$  eV, the optical transitions are predominantly contributed from  $\Sigma - \Sigma_1$  path where Weyl nodes are identified in previous literature [41]. At this energy, the major optical transitions are identified to be V2-C1 and V1-C2, which can be associated with transitions from states below the LWB to the UWB and from the LWB to state above the UWB. From 0.3 eV to 0.7 eV, the  $k$  space that contributes to  $|\tilde{\epsilon}_{11}|$  changes to  $\Sigma_1 - Z$ . The  $Z - \Gamma$  starts to play a significant role from 1.7 eV to 2.3 eV because of a collection of resonant bands near the high symmetry Z point. In the energy range from 2.3 to 3.5 eV, the predominant  $k$  space contribution to the dielectric function shifts to  $\Gamma - \Sigma$  because of the large joint density of states (JDOS).

Similarly, along the extraordinary direction of TaAs, 16 oscillators are fitted to the DFT derived dielectric function,  $|\tilde{\epsilon}_{33}|$ . At energy below 0.5 eV, the optical transitions occur mostly along  $\Sigma - \Sigma_1$ . Within 0.5 eV to 3.5 eV,  $\Gamma - X$  is the primary  $k$  space path that dominates the  $|\tilde{\epsilon}_{33}|$  as shown in the blue and dark green rectangles in **Fig. 3(b)**. Therefore, the origin of the macroscopic oscillators in TaAs can be attributed to certain pairs of bands in momentum space. For instance, a collection of bands along  $Z - \Gamma$  are resonant from 2.9 eV to 3.2 eV, which correspond approximately to oscillators at 3.0 eV (Expt.) and 2.9 eV (DFT). In **Figs. 3(c) and (d)**, the  $k$ -dependent dielectric constants for each pair of bands at resonance energies along ordinary and extraordinary directions are shown. Here, we take optical transitions V1-C2 and V2- C1 as an example, which are Ta ( $5d$ ) to Ta ( $5d$ ) transitions. Along the ordinary direction in **Fig. 3(c)**, the optical transitions V1- C2 and V2- C1 yield the largest  $|\tilde{\epsilon}|$  below 1 eV at  $\Gamma - \Sigma$ ,  $\Sigma - \Sigma_1$  and  $\Sigma_1 - Z$ .

Along the extraordinary direction in **Fig. 3(d)**, the optical transitions V1- C2 and V2-C1 dominate  $|\tilde{\epsilon}|$  below 0.5 eV along the  $\Sigma - \Sigma_1$  path. These differences highlight the anisotropic optical response and the energy range that a pair of bands can influence.

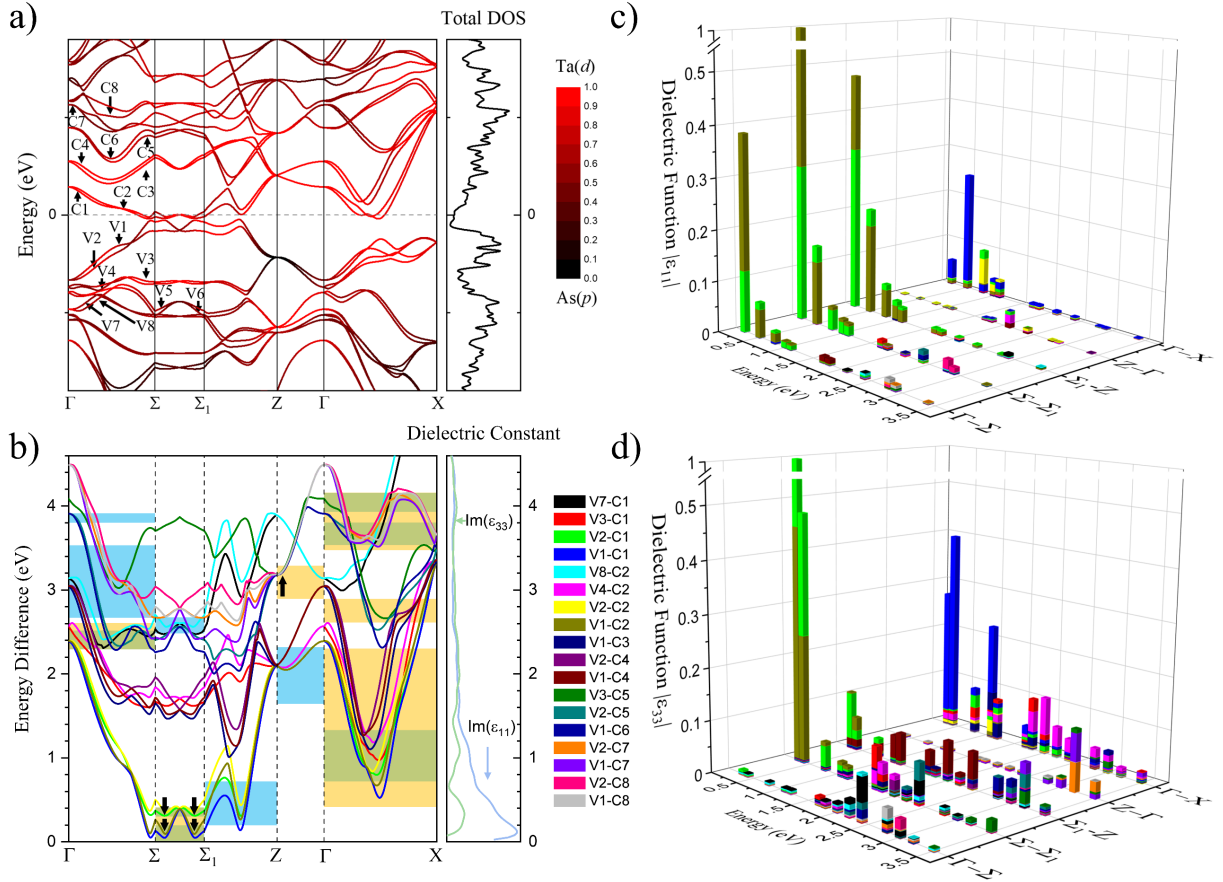


**FIG 3.** a) DFT-SOC band structure of TaAs. The color scale represents the relative band character of Ta ( $d$ ) (red) vs. As( $p$ ) (black) orbitals. b) The energy difference between selected pairs of bands contributing the most to the magnitude of the dielectric functions. The colored boxes highlight the paths and energy ranges that contribute the most to the dielectric function in that energy range. The blue, orange, and dark green boxes correspond to pairs of bands contributing the most to  $|\tilde{\epsilon}_{11}|$ ,  $|\tilde{\epsilon}_{33}|$ , and both, respectively. Arrows indicate Van Hove singularities that contribute to resonances. Normalized  $k$ -dependent contributions to the dielectric constants for the same pairs of bands as in (b) calculated along the c) ordinary and d) extraordinary directions, respectively using **Eq. (2)**. The color scale is the same as in panel (b).

### C. Resonances close to observed optical second harmonic generation energies

Since  $\chi_{333}^{(2)}$  is proportional to the product,  $\tilde{\epsilon}_{33}^2(\omega)\tilde{\epsilon}_{33}(2\omega)$ , and since resonances will enhance the linear dielectric permittivities, they will enhance the  $\chi_{333}^{(2)}$  [44]. A large  $\chi_{333}^{(2)}$  can be observed by a large transition dipole moment  $\mu$  for a linear resonance, or a resonance close to either  $\omega$  or  $2\omega$  state [43]. Therefore, the direct optical transition with photon energy close to either  $\omega$  or  $2\omega$  states will enhance the SHG response. Optical second harmonic generation (SHG) measurements were previously performed at various incident fundamental energies such as 0.7 eV and 1.55 eV, and large  $\chi_{333}^{(2)}$  coefficients were reported [26,27]. Experimental oscillators at 1.8 eV and 3.0 eV and DFT oscillators at 0.8, 1.7, 3.0, and 3.2 eV are close to the reported fundamental and SHG energies of interest, and thus likely resonantly enhancing the SHG. The  $\Gamma - X$  dominates the overall  $|\tilde{\epsilon}_{33}|$  from 0.5 eV to 2.3 eV. Major optical transitions occur at V1-C1 at 0.7 eV and V3-C1 at 1.55 eV. At  $2\omega = 3.1$  eV, the optical transition is located on the tail of 3.2 eV resonances contributed by a collection of bands at the Z point. In addition, there are contributions from Van Hove singularities (see next section) and larger  $\mu$ 's contributing to the SHG enhancement at 3.1 eV energy. All of these resonances can thus enhance the observed SHG.

### D. Van Hove Singularities and Weyl Point Contribution

A set of near-parallel flat bands or where there is a change in the slope of the  $E(k)$  relation can produce Van Hove singularities (VHS) and can give rise to large joint density of states (JDOS). [45–49] The VHS has been previously reported at the saddle points connecting two Weyl nodes. [24,50] **Figure 3(b)** plots the energy differences for several selected pairs of bands with strong resonances. Along the extraordinary direction, the VHS is confirmed as highlighted by the

dark arrows where  $\nabla_{\mathbf{k}}\varepsilon_g(\mathbf{k}) = 0$ . [47] Here,  $\mathbf{k}$  is the lattice momentum and  $\varepsilon_g$  is the energy gaps. By identifying the  $k$ -space momenta, the VHS are located at  $\Sigma - \Sigma_1$  below 0.4 eV and near high symmetry point  $Z$  at 3.2 eV. The resonances contributed by VHS are confirmed by macroscopic oscillators at 0.3 eV and 3.2 eV. Moreover, the collection of bands near  $Z$  at 3.2 eV further increases the JDOS. In addition, dipolar transition matrix elements are larger near the VHS as compared with the nearby momentum space. Therefore, the SHG detected at 3.1 eV is enhanced by direct optical transition, VHS and large transition matrix elements.

Motivated by the resonances near the Weyl points, we then examine the contributions of two different types of Weyl points to the dielectric functions. **Fig. 4** shows the anisotropic dielectric functions solely contributed by the Weyl points (WP1 and WP2). Along the ordinary direction, both Weyl points show a similar contribution to  $|\tilde{\varepsilon}_{11}|$  across the spectrum, and the magnitude of the dielectric functions tends to diminish after 0.2 eV. Along the extraordinary direction, the contribution to the  $|\tilde{\varepsilon}_{33}|$  from WP2 tends to dominate the total dielectric response within 0-0.5 eV, and the contribution declines above 1 eV. However, the contribution from WP1 remains negligible across the entire spectrum. The DFT results in this study agree well with previous conclusions performed in the low energy range (0-0.2 eV) using a linear band approximation [25]. Below 0.2 eV, the remaining dielectric function other than WP suggests dielectric resonances from trivial bands in TaAs. However, in NbAs, the contributions from trivial bands are small at low energies. This anisotropic behavior in the lower energy range can be understood as different dispersions at two Weyl points using the approximate expression for the matrix elements for interband transitions,  $\langle +\mathbf{k}|p_j|-\mathbf{k}\rangle^2 \propto \frac{1}{2}m^2(v_{F,+j}^2 + v_{F,-j}^2)$  [25]. Here,  $v_F$ ,  $k$  and  $p$  are Fermi velocity, wavevector, and transition dipole operator, respectively. Subscript  $j$  represents directions. Since the dispersion and Fermi velocity at WP2 along the polar axis is much



larger than that of WP1, the dipolar transition matrix elements at WP2 is therefore larger, yielding a higher dielectric response along the polar axis. However, at higher energies, such as in the visible range where many optical measurements are typically performed, the contribution to dielectric function from both the Weyl points is negligible.

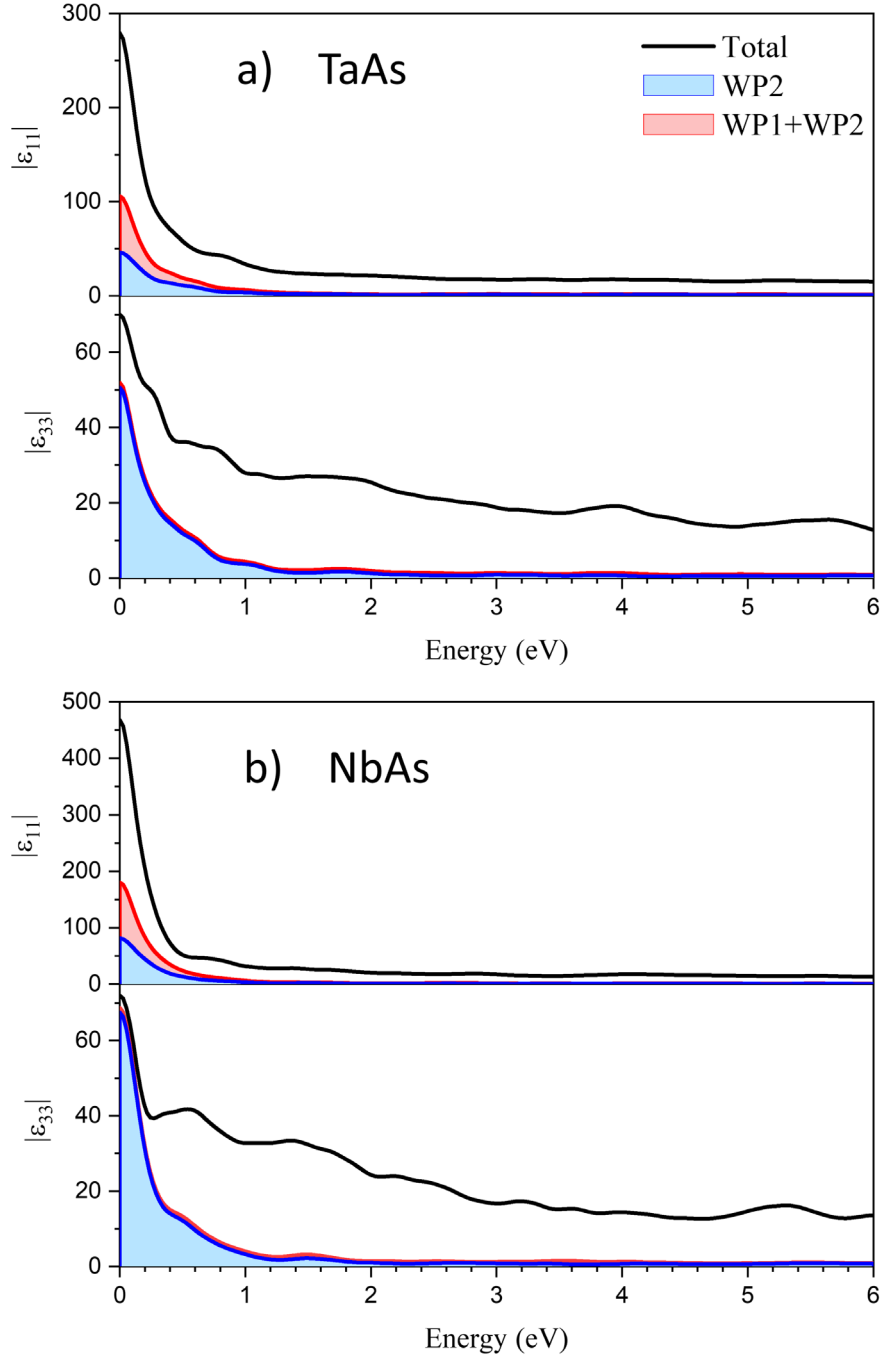


FIG 4. Contributions of two types of Weyl points to the magnitudes of dielectric functions  $|\tilde{\epsilon}|$ . a) Dielectric functions of TaAs. b) Dielectric functions of NbAs. The upper panel represents the ordinary direction, and the bottom panel represents the extraordinary direction. The black (entire

Brillouin zone), red (contribution from the 8 WP1 + 16 WP2), and blue (16 WP2 only) curves represent  $|\tilde{\epsilon}|$  contributions, as noted from different regions of the Brillouin zone.

#### IV. CONCLUSIONS

In summary, the eigen-cut TaAs and NbAs are used for the study to probe the anisotropic optical properties directly. Linear optical susceptibilities of TaAs and NbAs are measured by ellipsometry and confirmed by density functional theory (DFT). The oscillators and their parameters are extrapolated from both experiments and DFT, which show a reasonable agreement. At probing energies where many optical experiments are typically performed (near-infrared and visible), strong optical transitions are found due to large dipolar transition matrix elements, direct optical transitions, and Van Hove singularities. Furthermore, by evaluating the Weyl point contributions, WP2 strongly influences the dielectric function  $|\tilde{\epsilon}_{33}|$  below 0.5 eV, while the contribution from both the WPs on the dielectric function is insignificant above 1 eV. NbAs shares a similar response in terms of energy and momentum-resolved contributions to the dielectric spectrum. However, the contribution of the interband transitions below 0.2 eV to the extraordinary dielectric function is near completely ( $\sim 94\%$  in the limit of zero frequency) contributed by Weyl points in NbAs as compared with TaAs where the same contribution is at most  $\sim 72\%$ .

#### ACKNOWLEDGMENTS

R.Z. acknowledges useful discussions with Yoonsang Park, Hari Padmanabhan, Jingyang He, and Xinyu Liang. R. Z, L. M, Z. M, and V. G acknowledge support from the NSF MRSEC Center for Nanoscale Science, DMR-2011839. M.G. was supported by the DOE under grant no. DE-SC0012375. J.M.R was supported by the Army Research Office (ARO) under grant no.

W911NF-15-1-0017. Work at UCLA was supported by NSF DMREF program under the award NSF DMREF project DMREF-1629457.

## APPENDIX A: Parameters of Lorentz Oscillators from Ellipsometry and DFT

Based on **Eq. 1**, parameters of oscillators in TaAs and NbAs are extrapolated and summarized in **Table A. I-IV**. The spectroscopic range of ellipsometry covers the oscillators from 1.2 - 6 eV (1000 - 200 nm). The oscillators from DFT are fitted from 0 - 6 eV to obtain a complete spectroscopic range and to compare with the experimental results.

TABLE AI. Parameters for the Lorentz oscillators given by Eq. (1) for the ordinary dielectric function  $|\tilde{\epsilon}_{11}|$  for TaAs.  $\epsilon^\infty = 1.8$  (Expt.) and 1.8 (DFT),  $A_{UV} = 0.1$  (Expt). and 34.5 (DFT),  $E_{UV} = 6.6$  (Expt.) and 7.0 (DFT),  $A_{IR} = 10.0$  (Expt.),  $E_{IR} = 0$  (Expt.).

Oscillators	Expt. resonance (Broadening) (eV)	Expt. resonance amplitude (a.u.)	DFT Resonance (Broadening) (eV)	DFT resonance amplitude (a.u.)
1	1.0(0.8)	21.2	0.2(0.3)	200.7
2	1.8(0.5)	1.0	0.5(0.4)	41.9
3	2.9(4.0)	11.3	0.8(0.2)	8.2
4	3.7(0.5)	1.4	1.1(0.7)	20.9
5	4.1(0.4)	0.8	1.7(0.6)	9.0
6	4.8(2.2)	4.9	2.1(0.6)	6.1
7	5.7(1.0)	1.2	2.4(0.5)	7.9
8	6.8(2.0)	4.6	2.8(0.5)	4.3
9	-	-	3.4(1.0)	9.3
10	-	-	3.9(0.6)	5.0
11	-	-	4.4(0.7)	6.6
12	-	-	5.1(0.6)	3.1
13	-	-	5.5(1.8)	3.9
14	-	-	5.9(2.8)	4.1
15	-	-	6.0(2.2)	6.6

TABLE AII. Parameters for the Lorentz oscillators given by Eq. (1) for the ordinary dielectric function  $|\tilde{\epsilon}_{33}|$  for TaAs.  $\epsilon^\infty = 1.7$  (Expt.) and 1.9 (DFT),  $A_{UV} = 0.1$  (Expt.) and 49.8 (DFT),  $E_{UV} = 6.5$  (Expt.) and 6.9 (DFT),  $A_{IR} = 6.6$  (Expt.),  $E_{IR} = 0$  (DFT).

Oscillators	Expt. resonance (Broadening) (eV)	Expt. resonance amplitude (a.u.)	DFT Resonance (Broadening) (eV)	DFT resonance amplitude (a.u.)
1	1.2(0.5)	8.0	0.3(0.4)	12.4
2	1.8(0.8)	4.6	0.4(0.4)	14.9
3	2.2(0.2)	1.6	0.8(0.2)	2.4
4	2.8(0.3)	0.8	1.1(0.6)	15.6
5	3.0(4.4)	12.4	1.7(0.5)	8.3
6	4.1(0.8)	2.8	2.0(0.4)	6.5
7	6.2(4.1)	5.0	2.4(0.9)	13.5
8	-	-	2.8(0.3)	2.9
9	-	-	3.0(0.5)	6.1
10	-	-	3.2(0.3)	2.3
11	-	-	3.5(0.6)	5.4
12	-	-	4.0(0.7)	10.5
13	-	-	4.5(0.5)	4.3
14	-	-	5.1(0.3)	0.7
15	-	-	5.6(2.0)	13.3
16	-	-	5.7(0.6)	0.9

TABLE AIII. Parameters for the Lorentz oscillators given by Eq. (1) for the ordinary dielectric function  $|\tilde{\epsilon}_{11}|$  for NbAs.  $\epsilon^\infty = 1.4$  (Expt.) and 1.4 (DFT),  $A_{UV} = 1.4$  (Expt.) and 9.0 (DFT),  $E_{UV} = 6.7$  (Expt.) and 6.4(DFT),  $A_{IR} = 12.2$  (Expt.),  $E_{IR} = 0$  (DFT).

Oscillators	Exp. resonance (Broadening) (eV)	Exp. resonance amplitude (a.u.)	DFT Resonance (Broadening) (eV)	DFT resonance amplitude (a.u.)
1	1.1(0.2)	11.3	0.2(0.3)	389.3
2	1.7(2.4)	17.3	0.5(0.3)	29.2
3	3.0(0.9)	3.4	0.8(0.4)	15.3
4	4.4(1.5)	2.6	1.2(0.4)	10.4
5	5.9(5.6)	5.1	1.4(0.6)	7.1
6	-	-	1.8(0.5)	4.6
7	-	-	2.2(1.5)	8.6
8	-	-	2.9(0.4)	4.6
9	-	-	3.1(0.3)	2.0
10	-	-	3.8(0.5)	1.7
11	-	-	4.1(0.4)	4.0
12	-	-	4.6(0.6)	4.6
13	-	-	5.4(0.3)	1.6
14	-	-	5.7(1.3)	4.9

TABLE AIV. Parameters for the Lorentz oscillators given by Eq. (1) for the ordinary dielectric function  $|\tilde{\epsilon}_{33}|$  for NbAs.  $\epsilon^\infty = 2.3$  (Expt.) and 2.0 (DFT),  $A_{UV} = 3.4$  (Expt.) and 48.4 (DFT),  $E_{UV} = 6.7$  (Expt.) and 6.8 (DFT),  $A_{IR} = 8.3$  (Expt.),  $En\ IR = 0$  (DFT).

Oscillators	Exp. resonance (Broadening) (eV)	Exp. resonance amplitude (a.u.)	Theory Resonance (Broadening) (eV)	Theory resonance amplitude (a.u.)
1	1.5(1.2)	20.1	0.1(0.2)	66.6
2	1.9(0.2)	1.9	0.6(0.1)	3.5
3	2.6(1.5)	10.2	0.8(0.3)	10.8
4	3.5(0.7)	3.0	1.1(0.5)	12.8
5	4.6(2.8)	4.7	1.5(0.6)	11.7
6	5.5(0.8)	3.5	1.8(0.5)	11.6
7	6.4(1.0)	2.9	2.1(0.5)	8.9
8	-	-	2.4(0.5)	10.5
9	-	-	2.8(0.5)	7.7
10	-	-	3.2(0.5)	7.9
11	-	-	3.6(0.7)	6.9
12	-	-	4.1(0.7)	7.1
13	-	-	4.6(0.7)	4.9
14	-	-	5.1(0.6)	5.2
15	-	-	5.4(0.6)	9.7
16	-	-	6.0(0.7)	10.5

## APPENDIX B: ANISOTROPIC DIELECTRIC TENSOR IN NbAs: EXPERIMENTS AND DFT

**Fig. B1** shows the complete set of Expt. and DFT oscillators from 1.2-6 eV and 0-6 eV in NbAs. The black curve shows the total  $\epsilon''$  and the colored curves represent each oscillator. Like TaAs, there are mainly 14-16 oscillators (DFT) along each eigendirection from 0-6 eV. Strong resonances can be identified in the low energy range, which can be associated with the interband transition near the Weyl points. [51] **Figure B1(a)** shows Expt. and DFT resonances in NbAs along the ordinary direction, and similar resonances are mapped with the same colors purely as an approximate guide to the eye. Experimental oscillators at 1.1 eV can be approximately mapped one-to-one with DFT oscillators at 1.2 eV. But 1.7, 3.0, 4.4, and 5.9 eV oscillators (Expt.) each map a cluster of resonances captured by DFT. **Figure B1(b)** shows oscillators along the extraordinary direction. Resonances (Expt.) at 1.5 and 3.5 eV can be relatively mapped one-to-one with DFT oscillators at 1.5 and 3.6 eV, respectively. The broad resonances (Expt.) at 2.6 eV and 4.6 eV can be explained by a mixture of resonances (DFT) from 1.5-3.2 eV and 4.1-5.1 eV.



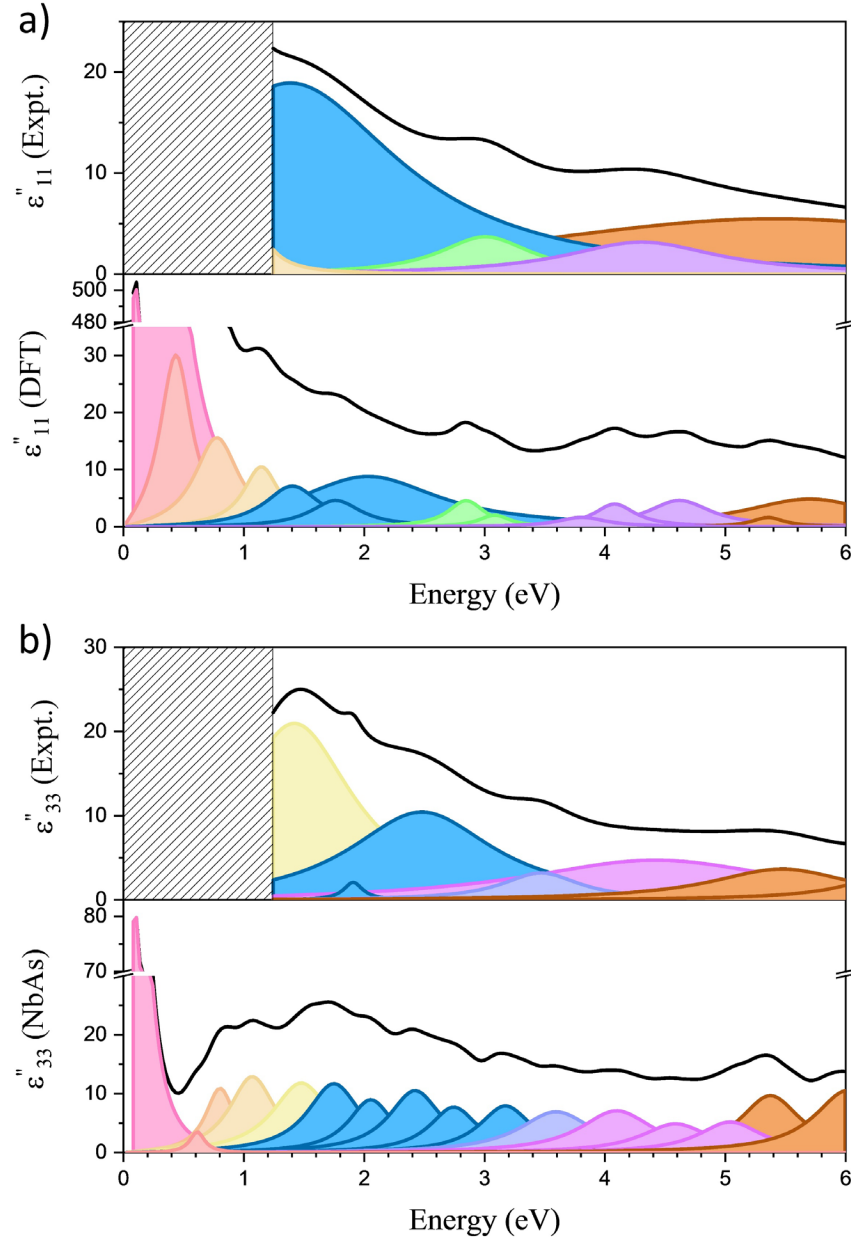


FIG B1. Detailed Lorentz oscillators for NbAs obtained from both experiments and DFT. a) Ordinary imaginary dielectric function. The hatched area indicates the energy range beyond the experimentally measured spectrum. b) Extraordinary imaginary dielectric function. The black curve is the total imaginary dielectric function. Colored resonance fits represent individual oscillators. In each subplot, similar colors of oscillators are approximately many-to-one mapping

from theory to experiments; they are only to be taken as a guide to the eye. The resonance energies and linewidths are given in **Tables A. III-IV**.

## **APPENDIX C: BAND STRUCTURE, BAND- AND MOMENTUM- RESOLVED DIELECTRIC RESPONSE IN NbAs**

In **Fig. 3(a)**, the calculated DFT-SOC band structure, and the resulting density of states for NbAs are shown. V1-10 and C1-8 are sequentially numbered valence and conduction bands. The band splitting by SOC in NbAs is smaller compared with TaAs due to the smaller atomic number of Nb [52]. The  $k$ -space momenta for WP1 and WP2 are calculated to be (0.891, 0.005, 0) and (0.012, 0.503, 0.306), respectively. Near the Fermi level, the states are mostly contributed by the hybridized Nb ( $d$ ) orbitals. Deep within the valence state, the states are mostly dominated by the As ( $p$ ) orbitals. In the case of optical excitation in the infrared (IR) and visible regimes, optical excitations in the system are dominated by Nb ( $d$ ) to Nb ( $d$ ) and As ( $p$ ) to Nb ( $d$ ) transitions.

The pairs of bands contributing most to the dielectric function at resonance energies are calculated using **Eq. (2)** and plotted in **Fig. C1(b)**. The colored rectangles in **Fig. C1(b)** show the pairs of bands within specific high symmetry paths that predominantly contribute to a certain dielectric constant value using the same scheme presented in **Fig. 3(b)**. From 0 to 0.4 eV, the optical transitions mainly arise from  $\Sigma - \Sigma_1$  near the Weyl nodes without SOC [41]. In this energy range, the primary optical transitions are identified to be V2-C1 and V1-C2. From 0.5 eV to 1 eV, the  $k$  space that contributes predominantly to  $|\tilde{\epsilon}_{11}|$  changes to  $\Gamma - X$ .  $Z - \Gamma$  becomes significant from 0.8 eV to 1.8 eV because of a cluster of resonant bands near high symmetry Z point, which corresponds to the macroscopic resonance (DFT) at 1.4 eV. The energy overlap from 0.8 eV to 1.0 eV suggests a near equal contribution from both  $Z - \Gamma$  and  $\Gamma - X$ . In the energy range from 1.8 to 3.4 eV, the predominant  $k$  space shifts to  $\Gamma - \Sigma$ .

Similarly, along the extraordinary direction of NbAs, 16 oscillators are fitted to the DFT derived dielectric function,  $|\tilde{\epsilon}_{33}|$ . At energies below 0.3 eV, the optical transitions occur mostly along  $\Sigma - \Sigma_1$ . In the 0.3 eV to 3.5 eV range,  $\Gamma - X$  is the primary  $k$  space that dominates the  $|\tilde{\epsilon}_{33}|$ . The macroscopic oscillators can then be correlated with pairs of energy bands in the momentum space. For example, a collection of bands at the high symmetry point  $Z$  are strongly resonant from 2.2 eV to 2.5 eV, which correspond to oscillators modeled at 2.6 eV (Expt.) and 2.4 eV (DFT). In the **Figs. C1(c)** and **(d)**, the  $k$ -dependent dielectric constants for each pair of bands at resonance energies along ordinary and extraordinary directions are shown. Similar to TaAs, we take optical transitions C2-V1 and C1-V2 as an example, which are mostly Nb ( $d$ ) to Nb ( $d$ ) transitions. Along the ordinary direction in **Fig. C1(c)**, the optical transitions C2-V1 and C1-V2 yield the largest  $|\tilde{\epsilon}|$  below 1 eV at  $\Gamma - \Sigma$ ,  $\Sigma - \Sigma_1$  and  $\Sigma_1 - Z$ . While along the extraordinary direction in **Fig. C1(d)**, the optical transitions C2-V1 and C1-V2 dominate  $|\tilde{\epsilon}|$  below 0.5 eV only at  $\Sigma - \Sigma_1$ .

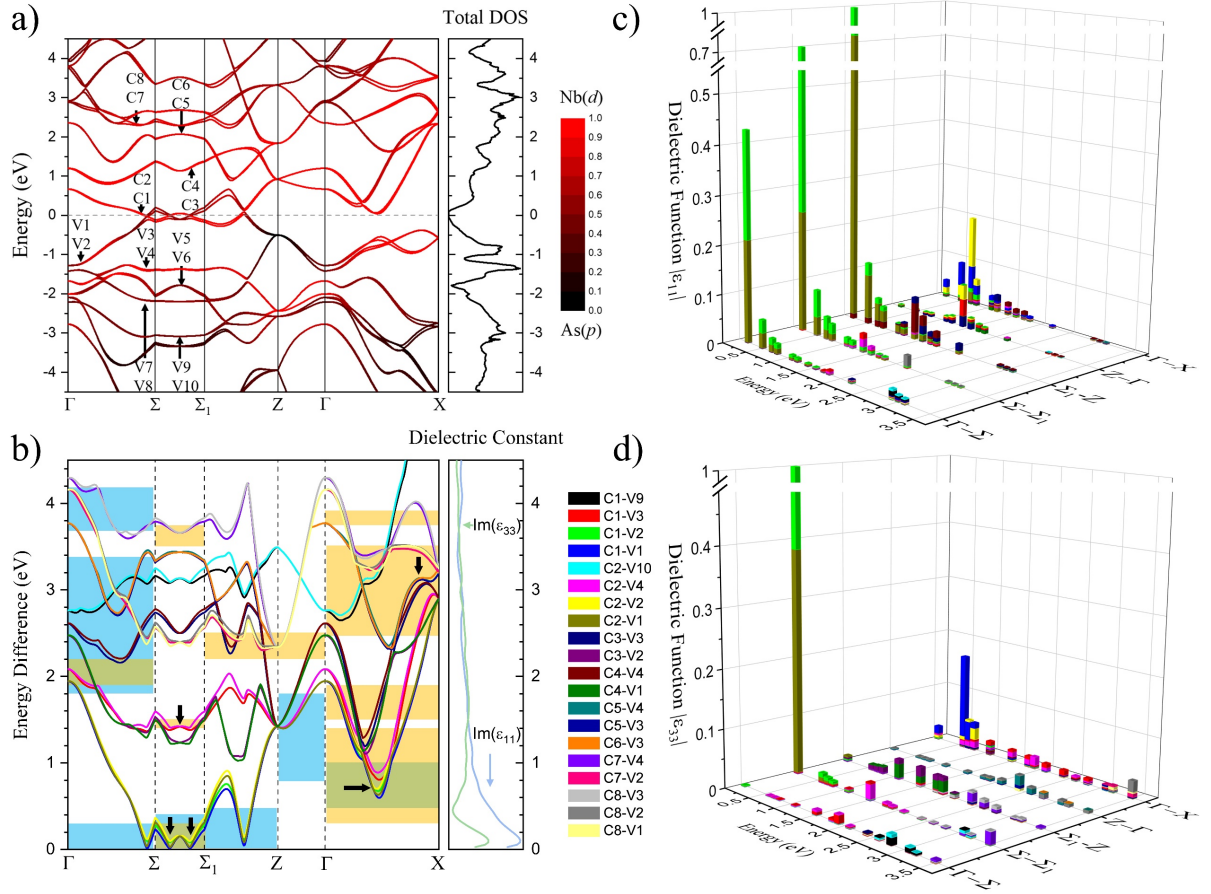


FIG C1. a) Band Structure of NbAs with SOC. The colored curve represents the ratio of states contributed by Nb ( $d$ ) orbital. b) The energy difference between selected pairs of bands contributing the most to the magnitude of the dielectric functions. The colored boxes highlight the paths and energy ranges that contribute the most to the dielectric function in that energy range. The blue, orange, and dark green boxes correspond to pairs of bands contributing the most to  $|\tilde{\epsilon}_{11}|$ ,  $|\tilde{\epsilon}_{33}|$ , and both, respectively. Arrows indicate Van Hove singularities that contribute to resonances. Normalized  $k$ -dependent contributions to the dielectric constants for the same pairs of bands as in (b) calculated from **Eq. (2)** along the c) ordinary and d) extraordinary directions, respectively. The color scale is the same as in panel (b).

## APPENDIX D: RESONANCES NEAR OBSERVED SECOND HARMONIC GENERATION ENERGIES AND VAN HOVE SINGULARITIES IN NbAs

By examining resonances near 0.7, 1.55, and 3.1 eV along the extraordinary direction, experimental oscillators at 1.5 eV and 2.6 eV are close to the energies of interest. DFT oscillators at 0.6, 0.8, 1.5, and 3.2 eV are near the reported energies. The  $\Gamma - X$  dominates the overall  $|\tilde{\epsilon}_{33}|$  at energies of interest, away from the Weyl points. The primary optical transition occurs between V1-C1 and V2-C2 at 0.7 eV. At 1.55 eV, the major optical transitions are V4-C2 and V3-C1. Two competing momentum spaces exhibit resonance at this range, where  $\Sigma - \Sigma_1$  exhibits highest  $|\tilde{\epsilon}_{33}|$  at 1.4-1.5 eV, but  $\Gamma - X$  shows the highest response in the rest of the energy range, as shown in **Fig. C1(b)**. Therefore, the enhancement at 1.55 eV is significantly contributed by the  $\Gamma - X$  path. At 3.1 eV, more bands are involved in the optical transitions, while V2-C7 and V3-C5 contribute more to the dielectric function than the contribution from other transitions.

Similar to TaAs, VHS contribute to resonances along the extraordinary direction, as highlighted by the black arrows in **Fig. C1(b)**. Below 0.2 eV, VHS can be observed at  $\Sigma - \Sigma_1$ . Near 0.7 eV, 1.55 eV, and 3.1 eV, where SHG measurements were performed in this family, VHS at  $\Sigma - \Sigma_1$  and  $Z - \Gamma$  are expected to enhance the SHG response. Moreover, the dipole moments  $\mu$  at dark arrows are larger than the rest of the  $k$ -space. Therefore, direct optical transitions, VHS, and large dipolar transition matrix elements can enhance  $|\tilde{\epsilon}_{33}|$  and further increase the SHG response near the SHG pumping and detecting energies.

## Reference

- [1] H. Weyl, *Elektron und Gravitation. I*, Z. Physik **56**, 330 (1929).
- [2] S.-Y. Xu, I. Belopolski, N. Alidoust, M. Neupane, G. Bian, C. Zhang, R. Sankar, G. Chang, Z. Yuan, C.-C. Lee, S.-M. Huang, H. Zheng, J. Ma, D. S. Sanchez, B. Wang, A. Bansil, F. Chou, P. P. Shibayev, H. Lin, S. Jia, and M. Z. Hasan, *Discovery of a Weyl Fermion Semimetal and Topological Fermi Arcs*, Science **349**, 613 (2015).
- [3] S.-M. Huang, S.-Y. Xu, I. Belopolski, C.-C. Lee, G. Chang, B. Wang, N. Alidoust, G. Bian, M. Neupane, C. Zhang, S. Jia, A. Bansil, H. Lin, and M. Z. Hasan, *A Weyl Fermion Semimetal with Surface Fermi Arcs in the Transition Metal Monopnictide TaAs Class*, Nature Communications **6**, 1 (2015).
- [4] H. Weng, C. Fang, Z. Fang, B. A. Bernevig, and X. Dai, *Weyl Semimetal Phase in Noncentrosymmetric Transition-Metal Monophosphides*, Phys. Rev. X **5**, 011029 (2015).
- [5] F. Arnold, C. Shekhar, S.-C. Wu, Y. Sun, R. D. dos Reis, N. Kumar, M. Naumann, M. O. Ajeesh, M. Schmidt, A. G. Grushin, J. H. Bardarson, M. Baenitz, D. Sokolov, H. Borrmann, M. Nicklas, C. Felser, E. Hassinger, and B. Yan, *Negative Magnetoresistance without Well-Defined Chirality in the Weyl Semimetal TaP*, Nature Communications **7**, 1 (2016).
- [6] L. X. Yang, Z. K. Liu, Y. Sun, H. Peng, H. F. Yang, T. Zhang, B. Zhou, Y. Zhang, Y. F. Guo, M. Rahn, D. Prabhakaran, Z. Hussain, S.-K. Mo, C. Felser, B. Yan, and Y. L. Chen, *Weyl Semimetal Phase in the Non-Centrosymmetric Compound TaAs*, Nature Physics **11**, 9 (2015).
- [7] B. Q. Lv, H. M. Weng, B. B. Fu, X. P. Wang, H. Miao, J. Ma, P. Richard, X. C. Huang, L. X. Zhao, G. F. Chen, Z. Fang, X. Dai, T. Qian, and H. Ding, *Experimental Discovery of Weyl Semimetal TaAs*, 8 (2015).

- [8] C. Shekhar, A. K. Nayak, Y. Sun, M. Schmidt, M. Nicklas, I. Leermakers, U. Zeitler, Y. Skourski, J. Wosnitza, Z. Liu, Y. Chen, W. Schnelle, H. Borrmann, Y. Grin, C. Felser, and B. Yan, *Extremely Large Magnetoresistance and Ultrahigh Mobility in the Topological Weyl Semimetal Candidate NbP*, Nature Physics **11**, 8 (2015).
- [9] I. Belopolski, S.-Y. Xu, D. S. Sanchez, G. Chang, C. Guo, M. Neupane, H. Zheng, C.-C. Lee, S.-M. Huang, G. Bian, N. Alidoust, T.-R. Chang, B. Wang, X. Zhang, A. Bansil, H.-T. Jeng, H. Lin, S. Jia, and M. Z. Hasan, *Criteria for Directly Detecting Topological Fermi Arcs in Weyl Semimetals*, Phys. Rev. Lett. **116**, 066802 (2016).
- [10] S.-Y. Xu, I. Belopolski, D. S. Sanchez, C. Zhang, G. Chang, C. Guo, G. Bian, Z. Yuan, H. Lu, T.-R. Chang, P. P. Shibayev, M. L. Prokopovych, N. Alidoust, H. Zheng, C.-C. Lee, S.-M. Huang, R. Sankar, F. Chou, C.-H. Hsu, H.-T. Jeng, A. Bansil, T. Neupert, V. N. Strocov, H. Lin, S. Jia, and M. Z. Hasan, *Experimental Discovery of a Topological Weyl Semimetal State in TaP*, Science Advances **1**, e1501092 (2015).
- [11] J. Hu, S.-Y. Xu, N. Ni, and Z. Mao, *Transport of Topological Semimetals*, Annual Review of Materials Research **49**, 207 (2019).
- [12] T. Liang, Q. Gibson, M. N. Ali, M. Liu, R. J. Cava, and N. P. Ong, *Ultrahigh Mobility and Giant Magnetoresistance in the Dirac Semimetal  $\text{Cd}_3\text{As}_2$* , Nature Materials **14**, 3 (2015).
- [13] X. Huang, L. Zhao, Y. Long, P. Wang, D. Chen, Z. Yang, H. Liang, M. Xue, H. Weng, Z. Fang, X. Dai, and G. Chen, *Observation of the Chiral-Anomaly-Induced Negative Magnetoresistance in 3D Weyl Semimetal TaAs*, Phys. Rev. X **5**, 031023 (2015).
- [14] E. Liu, Y. Sun, N. Kumar, L. Muehler, A. Sun, L. Jiao, S.-Y. Yang, D. Liu, A. Liang, Q. Xu, J. Kroder, V. Süß, H. Borrmann, C. Shekhar, Z. Wang, C. Xi, W. Wang, W. Schnelle, S.

- Wirth, Y. Chen, S. T. B. Goennenwein, and C. Felser, *Giant Anomalous Hall Effect in a Ferromagnetic Kagomé-Lattice Semimetal*, Nat Phys **14**, 1125 (2018).
- [15] Q. Wang, Y. Xu, R. Lou, Z. Liu, M. Li, Y. Huang, D. Shen, H. Weng, S. Wang, and H. Lei, *Author Correction: Large Intrinsic Anomalous Hall Effect in Half-Metallic Ferromagnet  $\text{Co}_3\text{Sn}_2\text{S}_2$  with Magnetic Weyl Fermions*, Nat Commun **9**, (2018).
- [16] A. Sakai, Y. P. Mizuta, A. A. Nugroho, R. Sihombing, T. Koretsune, M.-T. Suzuki, N. Takemori, R. Ishii, D. Nishio-Hamane, R. Arita, P. Goswami, and S. Nakatsuji, *Giant Anomalous Nernst Effect and Quantum-Critical Scaling in a Ferromagnetic Semimetal*, Nature Physics **14**, 11 (2018).
- [17] P. Li, J. Koo, W. Ning, J. Li, L. Miao, L. Min, Y. Zhu, Y. Wang, N. Alem, C.-X. Liu, Z. Mao, and B. Yan, *Giant Room Temperature Anomalous Hall Effect and Tunable Topology in a Ferromagnetic Topological Semimetal  $\text{Co}_2\text{MnAl}$* , Nature Communications **11**, 1 (2020).
- [18] Q. Ma, S.-Y. Xu, C.-K. Chan, C.-L. Zhang, G. Chang, Y. Lin, W. Xie, T. Palacios, H. Lin, S. Jia, P. A. Lee, P. Jarillo-Herrero, and N. Gedik, *Direct Optical Detection of Weyl Fermion Chirality in a Topological Semimetal*, Nature Physics **13**, 842 (2017).
- [19] B. Xu, Y. M. Dai, L. X. Zhao, K. Wang, R. Yang, W. Zhang, J. Y. Liu, H. Xiao, G. F. Chen, A. J. Taylor, D. A. Yarotski, R. P. Prasankumar, and X. G. Qiu, *Optical Spectroscopy of the Weyl Semimetal TaAs*, Physical Review B **93**, (2016).
- [20] B. Xu, Y. M. Dai, L. X. Zhao, K. Wang, R. Yang, W. Zhang, J. Y. Liu, H. Xiao, G. F. Chen, S. A. Trugman, J.-X. Zhu, A. J. Taylor, D. A. Yarotski, R. P. Prasankumar, and X. G. Qiu, *Temperature-Tunable Fano Resonance Induced by Strong Coupling between Weyl Fermions and Phonons in TaAs*, Nature Communications **8**, 14933 (2017).



- [21] H. W. Liu, P. Richard, Z. D. Song, L. X. Zhao, Z. Fang, G.-F. Chen, and H. Ding, *Raman Study of Lattice Dynamics in the Weyl Semimetal TaAs*, Phys. Rev. B **92**, 064302 (2015).
- [22] N. Sirica, R. I. Tobey, L. X. Zhao, G. F. Chen, B. Xu, R. Yang, B. Shen, D. A. Yarotski, P. Bownan, S. A. Trugman, J.-X. Zhu, Y. M. Dai, A. K. Azad, N. Ni, X. G. Qiu, A. J. Taylor, and R. P. Prasankumar, *Tracking Ultrafast Photocurrents in the Weyl Semimetal TaAs Using THz Emission Spectroscopy*, Phys. Rev. Lett. **122**, 197401 (2019).
- [23] B. Xu, Y. M. Dai, L. X. Zhao, K. Wang, R. Yang, W. Zhang, J. Y. Liu, H. Xiao, G. F. Chen, A. J. Taylor, D. A. Yarotski, R. P. Prasankumar, and X. G. Qiu, *Optical Spectroscopy of the Weyl Semimetal TaAs*, Physical Review B **93**, (2016).
- [24] S. Kimura, H. Yokoyama, H. Watanabe, J. Sichelschmidt, V. Süß, M. Schmidt, and C. Felser, *Optical Signature of Weyl Electronic Structures in Tantalum Pnictides  $TaP_n$  ( $P_n = P, As$ )*, Phys. Rev. B **96**, 075119 (2017).
- [25] D. Grassano, O. Pulci, A. Mosca Conte, and F. Bechstedt, *Validity of Weyl Fermion Picture for Transition Metals Monopnictides TaAs, TaP, NbAs, and NbP from Ab Initio Studies*, Sci Rep **8**, 3534 (2018).
- [26] L. Wu, S. Patankar, T. Morimoto, N. L. Nair, E. Thewalt, A. Little, J. G. Analytis, J. E. Moore, and J. Orenstein, *Giant Anisotropic Nonlinear Optical Response in Transition Metal Monopnictide Weyl Semimetals*, Nature Physics **13**, 350 (2017).
- [27] S. Patankar, L. Wu, B. Lu, M. Rai, J. D. Tran, T. Morimoto, D. E. Parker, A. G. Grushin, N. L. Nair, J. G. Analytis, J. E. Moore, J. Orenstein, and D. H. Torchinsky, *Resonance-Enhanced Optical Nonlinearity in the Weyl Semimetal TaAs*, Phys. Rev. B **98**, 165113 (2018).

- [28] Z. Li, Y.-Q. Jin, T. Tohyama, T. Iitaka, J.-X. Zhang, and H. Su, *Second Harmonic Generation in the Weyl Semimetal TaAs from a Quantum Kinetic Equation*, Phys. Rev. B **97**, 085201 (2018).
- [29] N. Nagaosa, T. Morimoto, and Y. Tokura, *Transport, Magnetic and Optical Properties of Weyl Materials*, Nat Rev Mater (2020).
- [30] S. Furuseth, K. Selte, A. Kjekshus, S. Gronowitz, R. A. Hoffman, and A. Westerdahl, *On the Arsenides and Antimonides of Tantalum.*, Acta Chem. Scand. **19**, 95 (1965).
- [31] S. Furuseth and A. Kjekshus, *The Crystal Structure of NbAs (Comments)*, Acta Cryst **17**, 1077 (1964).
- [32] T. Besara, D. A. Rhodes, K.-W. Chen, S. Das, Q. R. Zhang, J. Sun, B. Zeng, Y. Xin, L. Balicas, R. E. Baumbach, E. Manousakis, D. J. Singh, and T. Siegrist, *Coexistence of Weyl Physics and Planar Defects in Semimetals TaP and TaAs*, Phys. Rev. B **93**, 245152 (2016).
- [33] C.-L. Zhang, Z. Yuan, Q.-D. Jiang, B. Tong, C. Zhang, X. C. Xie, and S. Jia, *Electron Scattering in Tantalum Monoarsenide*, Phys. Rev. B **95**, 085202 (2017).
- [34] X. Huang, L. Zhao, Y. Long, P. Wang, D. Chen, Z. Yang, H. Liang, M. Xue, H. Weng, Z. Fang, X. Dai, and G. Chen, *Observation of the Chiral-Anomaly-Induced Negative Magnetoresistance in 3D Weyl Semimetal TaAs*, Phys. Rev. X **5**, 031023 (2015).
- [35] C.-L. Zhang, Z. Yuan, Q.-D. Jiang, B. Tong, C. Zhang, X. C. Xie, and S. Jia, *Electron Scattering in Tantalum Monoarsenide*, Phys. Rev. B **95**, 085202 (2017).
- [36] R. Sankar, G. Peramaiyan, I. P. Muthuselvam, S. Xu, M. Z. Hasan, and F. C. Chou, *Crystal Growth and Transport Properties of Weyl Semimetal TaAs*, J. Phys.: Condens. Matter **30**, 015803 (2017).

- [37] N. J. Ghimire, Y. Luo, M. Neupane, D. J. Williams, E. D. Bauer, and F. Ronning, *Magnetotransport of Single Crystalline NbAs*, J. Phys.: Condens. Matter **27**, 152201 (2015).
- [38] G. Kresse and J. Furthmüller, *Efficient Iterative Schemes for Ab Initio Total-Energy Calculations Using a Plane-Wave Basis Set*, Phys. Rev. B **54**, 11169 (1996).
- [39] J. P. Perdew, K. Burke, and M. Ernzerhof, *Generalized Gradient Approximation Made Simple*, Phys. Rev. Lett. **77**, 3865 (1996).
- [40] G. Kresse and D. Joubert, *From Ultrasoft Pseudopotentials to the Projector Augmented-Wave Method*, Phys. Rev. B **59**, 1758 (1999).
- [41] S.-M. Huang, S.-Y. Xu, I. Belopolski, C.-C. Lee, G. Chang, B. Wang, N. Alidoust, G. Bian, M. Neupane, C. Zhang, S. Jia, A. Bansil, H. Lin, and M. Z. Hasan, *A Weyl Fermion Semimetal with Surface Fermi Arcs in the Transition Metal Monopnictide TaAs Class*, Nat Commun **6**, 7373 (2015).
- [42] S.-M. Huang, S.-Y. Xu, I. Belopolski, C.-C. Lee, G. Chang, B. Wang, N. Alidoust, G. Bian, M. Neupane, C. Zhang, S. Jia, A. Bansil, H. Lin, and M. Z. Hasan, *A Weyl Fermion Semimetal with Surface Fermi Arcs in the Transition Metal Monopnictide TaAs Class*, Nat Commun **6**, 7373 (2015).
- [43] R. W. Boyd and D. Prato, *Nonlinear Optics*, 3 edition (Academic Press, Amsterdam ; Boston, 2008).
- [44] S. A. Denev, T. T. A. Lummen, E. Barnes, A. Kumar, and V. Gopalan, *Probing Ferroelectrics Using Optical Second Harmonic Generation*, Journal of the American Ceramic Society **94**, 2699 (2011).
- [45] A. J. Uzan, G. Orenstein, Á. Jiménez-Galán, C. McDonald, R. E. F. Silva, B. D. Bruner, N. D. Klimkin, V. Blanchet, T. Arusi-Parpar, M. Krüger, A. N. Rubtsov, O. Smirnova, M.

- Ivanov, B. Yan, T. Brabec, and N. Dudovich, *Attosecond Spectral Singularities in Solid-State High-Harmonic Generation*, Nat. Photonics **14**, 183 (2020).
- [46] A. H. Reshak, T. Ouahrani, R. Khenata, A. Otero-de-la-Roza, V. Luaña, and H. Baltache, *Density Functional Calculation for the First and Second Harmonic Generation of the Chalcopyrite Ga<sub>2</sub>AsSb*, Computational Materials Science **50**, 886 (2011).
- [47] L. Van Hove, *The Occurrence of Singularities in the Elastic Frequency Distribution of a Crystal*, Phys. Rev. **89**, 1189 (1953).
- [48] J. Trull, R. Vilaseca, J. Martorell, and R. Corbalán, *Second-Harmonic Generation in Local Modes of a Truncated Periodic Structure*, Opt. Lett., OL **20**, 1746 (1995).
- [49] M. Vandelli, M. I. Katsnelson, and E. A. Stepanov, *Resonant Optical Second Harmonic Generation in Graphene-Based Heterostructures*, Phys. Rev. B **99**, 165432 (2019).
- [50] C. J. Tabert and J. P. Carbotte, *Optical Conductivity of Weyl Semimetals and Signatures of the Gapped Semimetal Phase Transition*, Phys. Rev. B **93**, 085442 (2016).
- [51] X. Yuan, C. Zhang, Y. Zhang, Z. Yan, T. Lyu, M. Zhang, Z. Li, C. Song, M. Zhao, P. Leng, M. Ozerov, X. Chen, N. Wang, Y. Shi, H. Yan, and F. Xiu, *The Discovery of Dynamic Chiral Anomaly in a Weyl Semimetal NbAs*, Nature Communications **11**, 1 (2020).
- [52] F. Herman, C. D. Kuglin, K. F. Cuff, and R. L. Kortum, *Relativistic Corrections to the Band Structure of Tetrahedrally Bonded Semiconductors*, Phys. Rev. Lett. **11**, 541 (1963).

# **Supplementary Materials for Comprehensive Anisotropic Linear Optical Properties of Weyl Semimetals, TaAs and NbAs**

## **1. Synthesis Method**

Single crystals of TaAs and NbAs were grown by chemical vapor transport. The stoichiometric ratio of Ta (Nb) and As powder was thoroughly mixed, pressed into a pellet and sealed under a third atmospheric pressure of Ar in a quartz tube for the solid-state reaction. The tube was heated to 600°C at 50°C per hour, stayed for 10 hours, then heated to 1100°C at 50°C per hour, and finally dwelled for another 10 hours before water quenching. Three grams of such precursors are loaded with iodine pieces in a quartz tube. The density of the iodine was 18 mg/cm<sup>3</sup>. The quartz ampule was sealed under vacuum and put in a three-zone furnace for a four-week-long chemical vapor transport growth. The temperature was set to be 1050°C (950°C) at the source end and 950°C (850°C) at the sink end for TaAs (NbAs).

Powder X-ray data were collected using a PANalytical Empyrean diffractometer with Cu-K $\alpha$  radiation. As-grown surfaces of (020) can be identified and confirmed with the X-ray diffraction, which was polished to a larger size using 1-micrometer sandpapers and later used for the spectroscopic study.

## **2. Crystal Structure and Brillion Zone**

The crystal structure and Brillion zone of TaAs and NbAs are shown in **Fig. S1**. The yellow represents As atoms, and grey represents Ta or Nb atoms. The Brillion zone and high symmetry points are labeled in **Fig. S1(b)**.

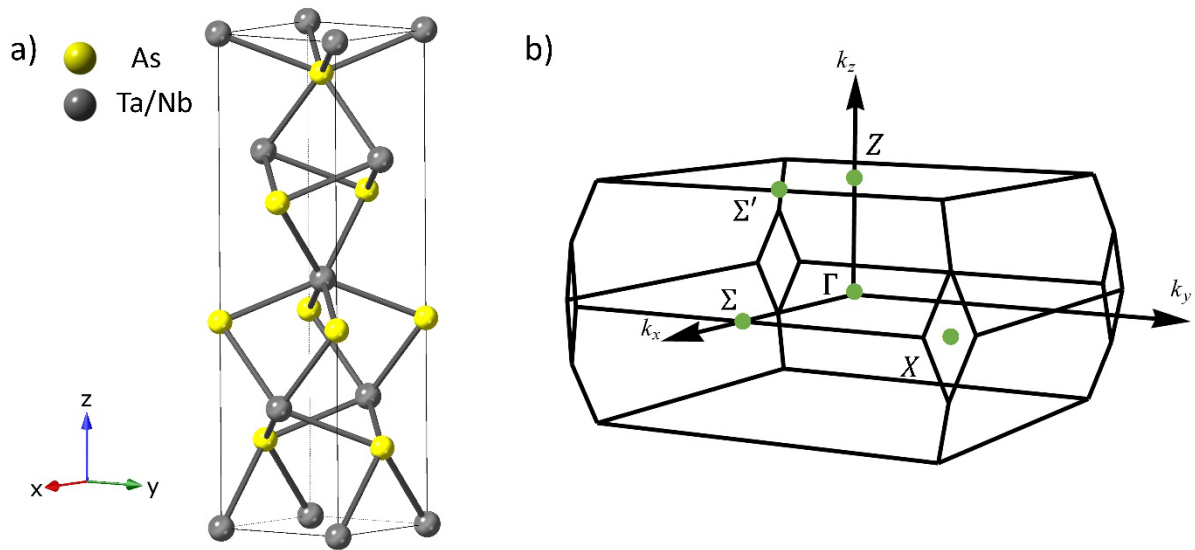


**FIG S1.** a) Crystal structure of TaAs and NbAs. b) The Brillion zone and high symmetry points of TaAs and NbAs.

### 3. Structure Characterization

Single crystalline TaAs and NbAs are confirmed using  $\theta$ - $2\theta$  X-ray diffraction (XRD), as shown in **Fig. S2**. The out-of-plane direction is confirmed to be (020).

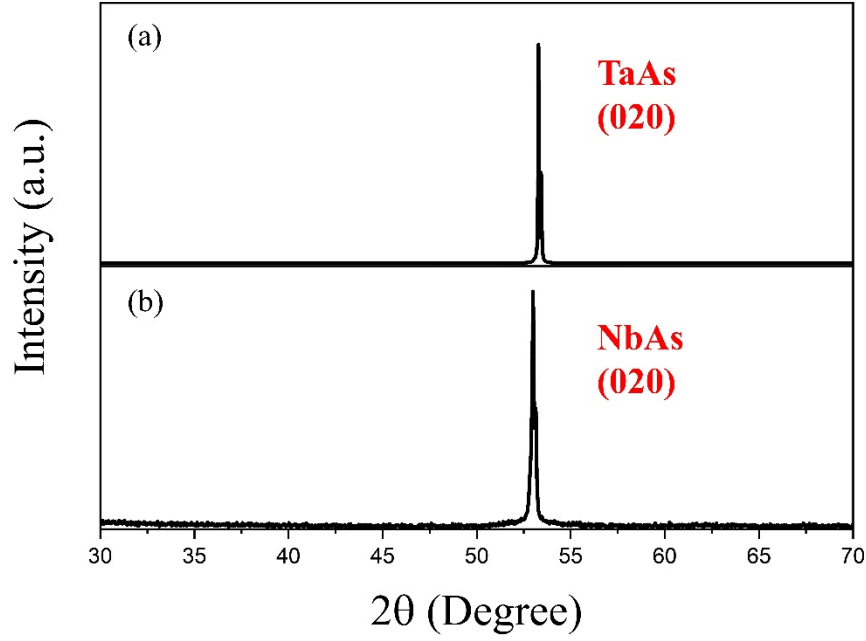


**FIG S2.** XRD of TaAs (020) and NbAs (020) plane. a) Experimental XRD of the TaAs (020) peak.  
b) Experimental XRD of NbAs (020) peak.

#### 4. Characterizations of Crystal Orientation

The crystals orientations are determined by combining Laue X-ray backscatter diffraction and the electron backscatter diffraction (EBSD). The raw crystals are shown in the upper panel of **Fig. S3**. By orientating the crystal axis parallel to the  $x$ - $y$ - $z$  coordinates ( $z$  as out-of-plane direction) in the EBSD system, the orientation maps are obtained with (020) intensity peaks along the  $z$ -direction, confirming the previous XRD pattern in **Fig. S2**. The [001] direction peaks along  $y$  for TaAs, and  $x$  for NbAs. The orientations are identified and aligned correctly for further anisotropic characterization.

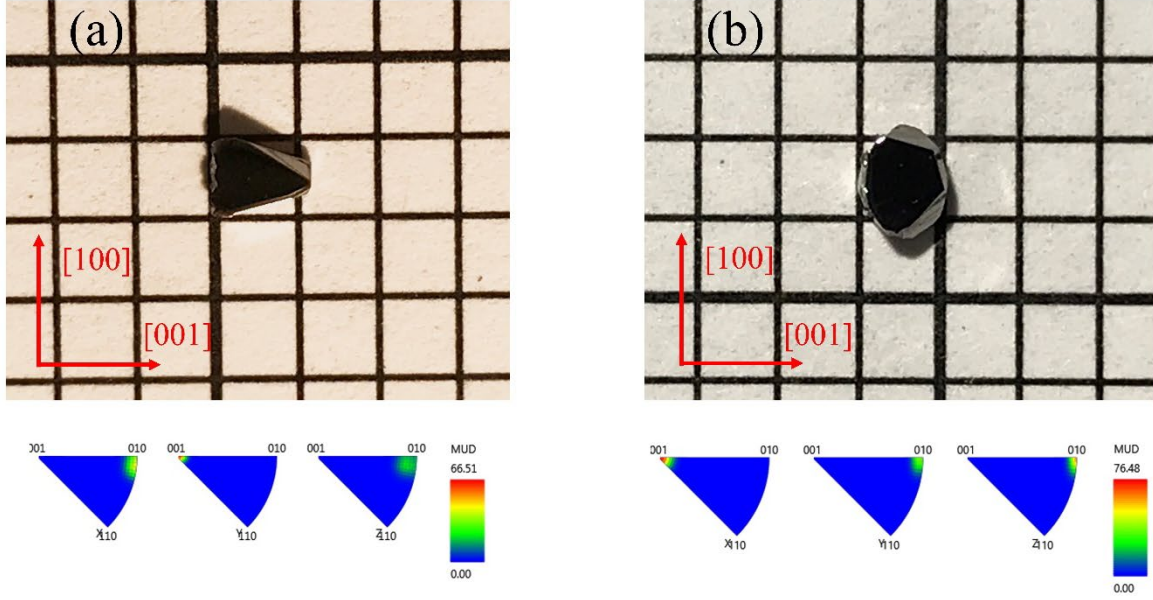


**FIG S3.** Optical images and inverse pole figures of synthesized a) TaAs and b) NbAs. The upper panel is the optical image of the studied crystals. The red arrows indicate crystallographic orientations. The length of the boxes is 2mm. The bottom panel is the inverse pole figures obtained from the EBSD. In the EBSD geometry, the  $[001]$  are oriented along y and x separately for TaAs and NbAs. The out-of-plane direction is along  $[010]$ , as shown in the z-direction.

## 5. Transport Properties

To characterize the quality of studied crystals, electrical and magnetoelectrical transport measurements were conducted with a standard four-probe method in a Quantum Design PPMS. The electric current was applied within the plane, while the magnetic field was along the out-of-plane direction for both TaAs and NbAs. To eliminate the non-symmetry of the contacts, the longitudinal resistivity ( $\rho_{xx}$ ) and Hall resistivity ( $\rho_{xy}$ ) are symmetrized using the formulas  $\rho_{xx}(H) = [\rho_{xx}(H) + \rho_{xx}(-H)]/2$  and  $\rho_{xy}(H) = [\rho_{xy}(H) - \rho_{xy}(-H)]/2$ , respectively.



The magnetic field dependent longitudinal resistivities of TaAs and NbAs are shown in **Fig. S4(a)**. In the low-temperature range ( $<100\text{K}$ ), Hall resistivity (**Fig. S4(b)** for TaAs; **Fig. S4(c)** for NbAs) shows large negative values and nonlinear field dependences and SdH oscillations, indicating both electrons and holes are involved in transport and electrons make dominant contributions to transport. Shubnikov–de Haas (SdH) oscillations are clearly observed at 2K in both field sweep measurements of longitudinal and Hall resistivity, shown in **Figs. S4(a), (b) and (c)**.

For TaAs, We have estimated the carrier densities and mobilities of low temperatures through the fits of longitudinal and Hall resistivity at 10K by a two-band model:  $n_e(10\text{K}) = 7.12 \times 10^{23} \text{ m}^{-3}$  and  $n_h(10\text{K}) = 5.56 \times 10^{23} \text{ m}^{-3}$ , and mobilities  $\mu_e(10\text{K}) = 6.04 \text{ m}^2\text{V}^{-1}\text{s}^{-1}$  and  $\mu_h(10\text{K}) = 2.54 \text{ m}^2\text{V}^{-1}\text{s}^{-1}$ . All these results above are comparable with previously reported data of TaAs single crystals [1–3]. In NbAs, strong SdH oscillation is also observed. Compared with TaAs, the Hall signal of NbAs at 2K is more linear and can be analyzed by a single-band model. Similar to the previous report [5], the electron carrier density and electron mobility of the NbAs crystal is  $n_e(10\text{K}) = 2.7 \times 10^{25} \text{ m}^{-3}$  and  $\mu_e(10\text{K}) = 83.5 \text{ m}^2\text{V}^{-1}\text{s}^{-1}$ , respectively.

The fitting of TaAs transport data is presented in **Fig. S4(d)**. The fitting of the low-temperature magnetoelectrical transport data is based on a simplified two-band model, where only one electron band and one hole band are considered. The longitudinal resistivity ( $\rho_{xx}$ ) and transverse resistivity ( $\rho_{xy}$ ) can be described as [4]

$$\rho_{xx} = \frac{(n_e\mu_e + n_h\mu_h) + (n_e\mu_e^2 + n_h\mu_h^2)B^2}{(n_e\mu_e + n_h\mu_h)^2 + \mu_h^2\mu_e^2(n_h - n_e)^2B^2} \cdot \frac{1}{e} \quad (\text{S1})$$

$$\rho_{xy} = \frac{(n_h\mu_h^2 - n_e\mu_e^2) + \mu_h^2\mu_e^2(n_h - n_e)B^2}{(n_e\mu_e + n_h\mu_h)^2 + \mu_h^2\mu_e^2(n_h - n_e)^2B^2} \cdot \frac{B}{e} \quad (\text{S2})$$

where  $n_e$  ( $n_h$ ) and  $\mu_e$  ( $\mu_h$ ) are the density and mobility of the electron (hole) band, respectively. To constrain the freedom of the fitting, in this work, the relationship between  $n_e$  and  $n_h$  is estimated by the linear fitting of the  $\rho_{xy}$  in the high-field range as  $\rho_{xy} = \frac{1}{n_h - n_e} \cdot \frac{B}{e}$  [2]. The fitting of NbAs transport data is presented in **Fig. S4(e)**. The fitting of the low-temperature magnetoelectrical transport data of NbAs is based on a single band approximation. The carrier density is described by  $n = \frac{1}{eR_H}$ , where  $R_H$  is the Hall coefficient. The mobility is further given by  $\mu = \frac{1}{en\rho_{xx}(0T)}$ , where  $\rho_{xx}(0T)$  is the longitudinal resistivity at zero magnetic field.

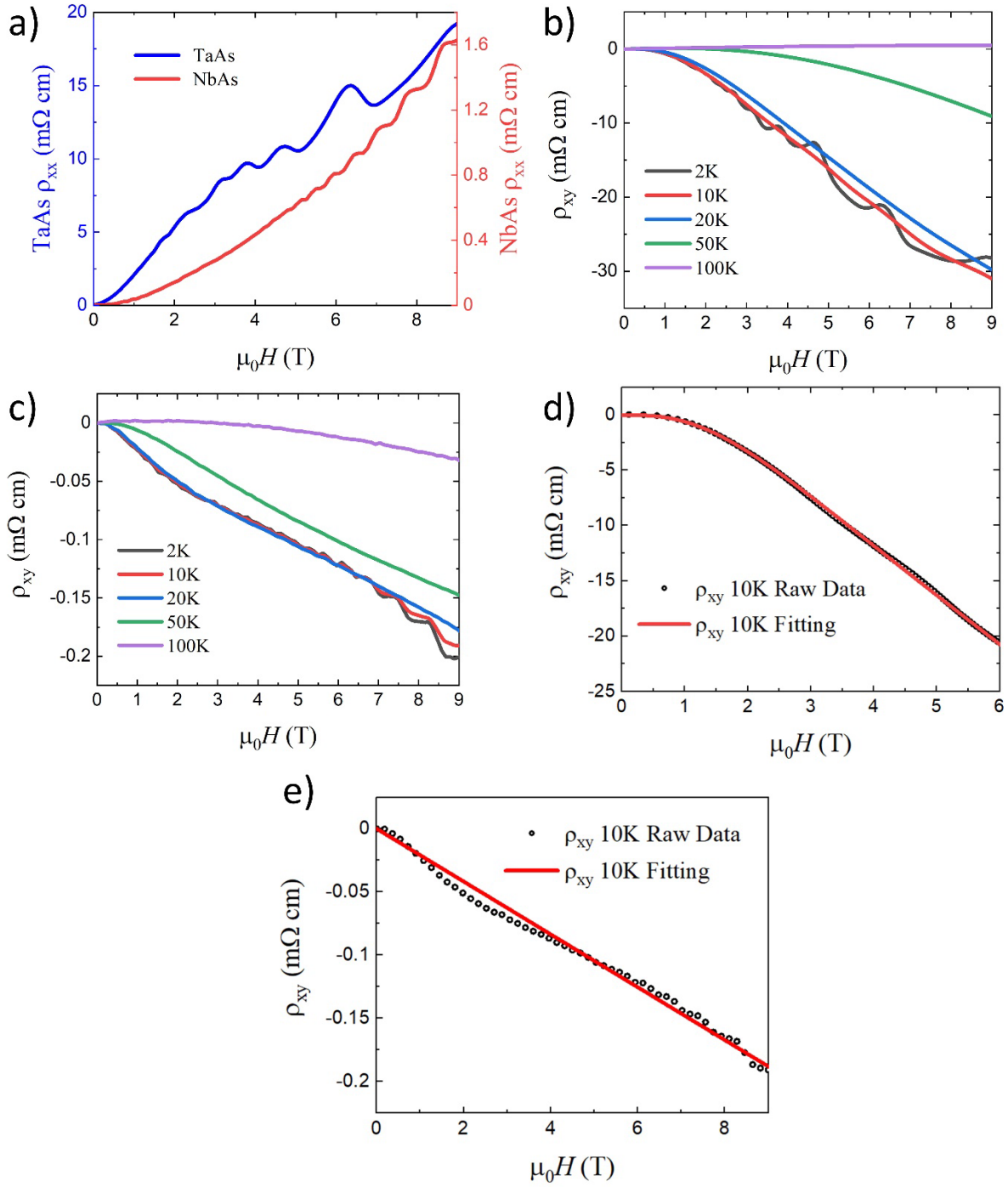


**FIG S4.** Transport Properties of TaAs and NbAs. (a) The magnetic field dependent longitudinal resistivity of TaAs and NbAs at 2K. The Hall resistivity versus magnetic fields and 50 to 2K in

TaAs (b) and NbAs (c). (d) The two-band model fitting of Hall resistivity for TaAs at 10K. (e) The single-band model fitting of Hall resistivity of NbAs at 10K.

## Reference

- [1] X. Huang, L. Zhao, Y. Long, P. Wang, D. Chen, Z. Yang, H. Liang, M. Xue, H. Weng, Z. Fang, X. Dai, and G. Chen, *Observation of the Chiral-Anomaly-Induced Negative Magnetoresistance in 3D Weyl Semimetal TaAs*, Phys. Rev. X **5**, 031023 (2015).
- [2] C.-L. Zhang, Z. Yuan, Q.-D. Jiang, B. Tong, C. Zhang, X. C. Xie, and S. Jia, *Electron Scattering in Tantalum Monoarsenide*, Phys. Rev. B **95**, 085202 (2017).
- [3] R. Sankar, G. Peramaiyan, I. P. Muthuselvam, S. Xu, M. Z. Hasan, and F. C. Chou, *Crystal Growth and Transport Properties of Weyl Semimetal TaAs*, J. Phys.: Condens. Matter **30**, 015803 (2017).
- [4] R. G. Chambers, *Electrons in Metals and Semiconductors* (Springer Netherlands, 1990).
- [5] N. J. Ghimire, Y. Luo, M. Neupane, D. J. Williams, E. D. Bauer, and F. Ronning, *Magnetotransport of Single Crystalline NbAs*, J. Phys.: Condens. Matter **27**, 152201 (2015).